Engineering Structures 238 (2021) 112251

Contents lists available at ScienceDirect

Engineering Structures

journal homepage: www.elsevier.com/locate/engstruct

Behaviour of concrete beams reinforced using basalt and steel bars under fire exposure

Ahmed Hassan [a,*], Fouad Khairallah [b], Hend Elsayed [c], Amany Salman [b], Hala Mamdouh [b]

[a] Department of Civil Engineering, Beni-Suef University, Egypt
[b] Department of Civil Engineering, Helwan University, Egypt
[c] M.Sc. Student, Department of Civil Engineering, Helwan University, Egypt

ARTICLE INFO

Keywords:
BFRP
Fire exposure
Flexural
Ductility
ANSYS

ABSTRACT

Basalt bars for concrete reinforcement, known as basalt fiber-reinforced polymers (BFRPs), are new natural inorganic materials with distinct mechanical properties that have been used recently in the construction field. Generally, the FRPs bars have no yield before the brittle failure as steel bars and their behavior, when exposed to fire, is still under investigation, this paper presents an experimental and theoretical study to get more knowledge about the characteristics and the fire resistance of a concrete beam reinforced using BFRPs and BFRPs mixed with steel bars. Eight half-scale concrete beams were constructed and tested up to failure at room temperature and under direct fire at 500 °C for 2 h. The basalt-to-steel percentage is the main parameter of this study. The BFRP-to-main-steel-bar replacement percentages are 100%, 67%, and 33% as three tension reinforcement bars were used. The results are discussed in terms of load capacity, cracking behaviour, and failure modes. Moreover, the experimental results are compared with theoretical calculations according to the ACI code and with numerical results obtained using the ANSYS finite element program. The results show that the beams with both steel and basalt reinforcement showed a better shear strength, enhanced crack stiffness, and lower degree of brittleness at failure. Our results also showed that the BFRPs beams yielded a better degradation resistance when the beams were exposed to fire as the failure load reduction factor for the BFRPs beam was 6.17% compared with that of steel beam which was 22.32%. More studies are needed to justify our observations in details and determine their applicabilities under different conditions.

1. Introduction

Generally, there were three common types of fiber-reinforced polymers (FRPs) (Aramid, Carbon, and Glass) and there is the relatively new Basalt fiber. Manufacturing technology based on dragging a material through a group of orifices to produce fiber strands, followed by immersing the latter in a resin and forming them in the shape of wrapped smooth bars, as well as performing roving to create ribbing, has been proposed [1]. Fiber-reinforced polymers (FRPs) are anisotropic materials that imply different mechanical properties in longitudinal and transverse directions as the longitudinal properties are governed by the fiber-properties whereas the transverse and shear properties are governed by the resin-properties [2]. BFRPs bars have become a useful replacement for conventional reinforcement in the construction industry and as external reinforcement for the strengthening of concrete structures; they demonstrate good resistance to environmental factors and have a high load capacity [3–5]. BFRPs enable a better life cycle structure owing to their high corrosion resistance [6–8]. BFRPs used in concrete structural elements such as foundations, breakwaters, and other seaside structures, as well as tanks in sewage treatment plants subjected to harsh environmental effects exhibit good resistances to chemical aggressiveness and fire [9,10]. Jongsung et al., [11] investigated heat resistance of fiber samples (glass, carbon, and basalt) which heated in a high-temperature oven for 2 h at 100, 200, 400, 600, and 1200 °C. They found that the basalt fiber kept about 90% of the normal temperature strength after exposure at 600 °C for 2 h whereas the carbon and the glass fibers did not maintain their volumetric integrity. This high heat resistance is due to the material characteristics of natural basalt rocks, which nucleates at high-temperature. BFRPs bar has a higher tensile strength than steel bars; moreover, their lower bulk density affords a reduced total structure weight [12,13]. The elastic modulus of BFRP bars is five times smaller than the coefficient of elasticity of steel bars, thereby resulting in a greater reduction in the cross-section stiffness of BFRPs after cracking [14]. In beams, the tensile strength of concrete relies on the tension stiffening effect (due to the bond of

* Corresponding author.

https://doi.org/10.1016/j.engstruct.2021.112251
Received 24 June 2020; Received in revised form 20 February 2021; Accepted 13 March 2021

Nomenclature

FRPs	*Fiber reinforced polymers*
BSRPs	*Basalt fiber reinforced polymers*
RC	*Reinforced concrete*
f_{cu}	*Cube compressive strength of concrete, N/mm^2*
fc'	*Cylinder compressive strength concrete, N/mm^2*
f_r	*Tensile cracking strength of concrete N/mm^2*
G1	*Group number one at room temperature*
G2	*Group number two under fire exposure*
S	*Beam with steel bars only*
1S-2B	*One steel bar, and two basalt bars*
2S-1B	*Two steel bars, and one basalt bar*
P_{cr}	*Cracking load, kN*
P_f	*Ultimate load, kN*
Δ_{cr}	*Cracking displacement, mm*
Δ_f	*failure displacement, mm*
Δ_y	*Yielding displacement, mm*
K_i	*Initial stiffness, kN/mm*
EX	*Modulus of elasticity of concrete*
PRXY	*Poisson's Ratio*
βo	*Shear transfer coefficients for an open crack*
βc	*Shear transfer coefficients for a closed crack*
a	*Shear span, mm*
I_g	*Gross moment of inertia, mm^4*
I_{cr}	*Cracked moment of inertia, mm^4*
I_e	*Effective moment of inertia, mm^4*
M_{cr}	*Cracking moment, N.mm*
M_a	*Applied moment, N.mm*
β_d	*Reduction coefficient*
ρ_{fb}	*Balanced reinforcement ratio of FRP beams*
β_1	*Factor depending on concrete strength*
E_f	*Longitudinal modulus of elasticity of FRP, N/mm^2*
ε_{cu}	*Ultimate compressive strain of concrete*
f_{fu}	*Design tensile strength of FRP considering reductions for service environment, N/mm^2*
f_f	*Design tensile strength of FRP bar, N/mm^2*

concrete and reinforcing bars through cracks) [15,16]. The tension stiffening action depends on the percentage of un-cracked moments of inertia to the element's cracked moment of inertia. The moment of inertia at cracked cross-sections in basalt-reinforced beams is approximately four times smaller than that in beams with steel reinforcement. Consequently, the serviceability analysis detects significantly higher strains in concrete, beam deflections, and width of cracks [17,18]. For deflection calculations, researchers have introduced factors to modify the traditional Branson's equation used in design codes to compute the deflections of beams reinforced with FRPs [19,20]. Meanwhile, other researchers have suggested a modified equivalent moment of inertia obtained from curvatures [21,22]. BFRP bars exhibit good thermal resistance and excellent performance under a rapid weathering test but fail to provide sufficient strength after being exposed to alkalis [3]. In addition, BFRPs demonstrate excellent freezing-and-thawing resistance [23] and good resistance to antagonistic acidic environments. The mechanical performances of the BFRP bars used in this study were favorable [24,25]. Furthermore, excellent bond strength has been reported for BFRP bars with concrete [26]. Reduction in concrete strength for different levels and durations of fire exposure has been reported [27].

The decline in the compressive strength of concrete becomes more rapid, i.e. drops by 50–60% when the temperature ranges between 300 and 500 °C [28,29]. An increase in concrete fire resistance by a protection layer or additives comprising carbon nanotubes in the concrete mix has been reported [30,31]. The mechanical properties of concrete reinforced with FRP bars differ according to fire exposure temperature. To use FRPs in structural applications, design codes and specifications are necessitated. However, information regarding the effect of elevated temperatures on FRPs is minimal. The manner of this combination through exposure to fire is complex and with limited data. Studies regarding the flexural behaviour of BFRP bars are insufficient, and most of them were conducted on small-scale Reinforced concrete beams. Herein, a report concerning the gathering of steel bars with BFRPs under fire exposure is presented.

2. Research objective

In this research the chosen rate of fire is (500 °C for 2 h) as it high enough to represent a fire event, also the concrete has a lower coefficient of thermal conductivity so the movement of heat through it is slow and thus the reinforcement inside it is protected, this rate ensures reaching this temperature to the core of concrete and the internal reinforcement. The main purposes of this research are:

- Studying experimentally the effects of using different ratios of steel bars with basalt bars in the same beam at the normal temperature (25 °C) and under fire exposure (500 °C for 2 h) on the load capacity, crack pattern, and failure type.
- Simulating behaviour of beams tested at room temperature using finite element program ANSYS package
- Theoretical calculations for beam specimens at room temperature.

Throughout this research, the results may provide fundamental information about the performance of beams reinforced using both steel and basalt bar as a flexural reinforcement and be able to predict their response under fire exposure.

3. Experimental programme

3.1. Materials

Experimental concrete mixes were prepared to yield a design compressive strength (f_{cu}) of 42.2 MPa and 35 MPa after 28 days at room temperature and at 500 °C, respectively. Concrete was produced by adjusting the size of thin and rough aggregates and increasing the quantity of cement paste to achieve high workability and reduce the risk of separation during the placing of concrete. After many attempts of producing the concrete mixes, the final ratios of the contents used for the mixing concrete are as shown in Table 1. The components were mixed using a cylinder tilting rotary mixer. The coarse aggregates, fine aggregates, and cement were dry mixed. Subsequently, water was added at regular intervals into the concrete blend after measuring the amount of cement, and the cement–water ratio was 0.5. The concrete mix was blended for two more minutes, resulting in a homogeneous concrete mixture. From the concrete mixture, eight cubes measuring 150 mm × 150 mm × 150 mm were cast to determine the compressive strength, and six cylinders measuring 150 mm × 300 mm were cast to measure the splitting tensile strength. The casting and curing processes were performed according to the procedures stipulated in the ECP standard

Table 1
Proportions of Components in Concrete Mixture.

Compressive Strength f_{cu} (MPa)	Water–Cement Ratiow/c	Cement Content (kg/m^3)	Coarse Aggregates (kg/m^3)	Fine Aggregates (kg/m^3)
42.4	0.5	350	1200	640

specification [32,33] (see Table 2).

Different reinforcement types were used in this study. High deformed steel bars of 10 mm diameter were used as top reinforcement and (steel and basalt) bars of 10 mm diameter were used as bottom reinforcement, and mild smooth steel 6 mm diameter was used as stirrups. To evaluate the axial tensile strength, at least three samples of each bar type were tested. Electrical strain gauges were bonded at the middle of each bar to measure the strain in the bars during the test. As shown in Fig. 1, the test was performed using a Shimadzu machine at the strength of the materials laboratory at Helwan University. The stress-strain curves of the tested bars are shown in Fig. 2.

Basalt Fiber Reinforced Polymer wrap used in this research was provided by the national center for quality supervision and test of building engineering (BETC-CL2-2014–311(A)). Table 3 includes the properties of basalt bars (see Table 4).

3.2. Preparing test specimens

Eight reinforced concrete beam specimens measuring 150 mm × 300 mm were tested in this study, with a total span of 1800 and 1650 mm in the center-right support and center-left support, respectively. The beam specimens were classified into two groups (G1, G2) according to the fire degree. The first specimen was reinforced using three steel bars, the second specimen using two steel bars and one BFRP bar, the third specimen using one steel bar and two BFRP bars, and the fourth specimen using three BFRP bars. The second group of specimens was the same as the first group, but the specimens were exposed to fire at a temperature of 500 °C, as shown in Table 3. Conventional 6-mm-diameter steel stirrups spaced at 70 mm were applied on the shear span. For the top reinforcement, two 10-mm steel bars were used to support the stirrups. The details of the reinforcement and the cross-section of the tested beams are illustrated in Fig. 3. Reinforcement cages were prepared and eight clean smooth wooden forms were used for casting all the test specimens as shown in Fig. 4.

All beam specimens were cured regularly by a sprinkling of water and covered by sackcloth to prevent moisture release from the concrete surface until the date of testing. Cubes and cylinders were curing by immersing them in water.

3.3. Fire exposure system

A steel furnace with seven burners lined parallel to each other was used with dimension 2000 mm × 2000 mm × 600 mm; the furnace was heated to the required temperature, i.e. (500 °C) and then kept at this temperature for 2 h. The beams, cubes, and cylinders subjected to direct fire are shown in Fig. 5. The used regime for cooling the fire beams was air.

3.4. Experimental setup and testing

All the beam specimens were subjected to two-point loading under an incremental force control which increased by 2kN per grade until cracks appearing, and then 4kN per grade up to the failure load. During the loading tests, load cells were used to measure the applied load, three linear variable differential transducers (LVDT) were used to measure the deflection (the first one at mid-span, the second followed it by 200 mm (under loading point), and the third followed it by (625) mm), sensors were used to prevent damage during the tests, and electrical strain gauges (60 mm length) were attached to measure the reinforcement strain. The strain gauges were fixed on the center of the middle bar in case of similar bars. However, in the case of reinforcement with two different types of bars (1S-2B), two strain gauges were used one in the middle of the steel bar and the other at the middle of the basalt bar. The digital load cell of capacity 550kN was adopted to measure the applied load, the load increments, and the displacements were read directly from the data recorder. The crack growth of the specimens during loading and at the time of failure was observed. The test setup and instrumentation are illustrated in Fig. 6.

4. Results and discussion

4.1. Cracking load and ultimate load

Table 5 shows the results of all tested beams, including the cracking load and its corresponding deflections (P_{cr} and Δ_{cr}) as well as the ultimate load and its corresponding deflection (P_f and Δ_f). Furthermore, the failure patterns of the BFRP and steel RC tested beams were observed. Fig. 7 illustrates the effect of BFRP reinforcement percentage on the cracking and ultimate loads for all specimens at 25 °C and 500 °C.

Overall, the quick glance of Table 5 and Fig. 7 reveal that there is a direct relation between BFRP reinforcement ratio and corresponding load capacity values at two cases of study (room temperature 25 °C and at 500 °C), this is due to the extremely high tensile strength of BFRP bars as the used basalt bars in this research have a tensile strength about three times that of the steel bar and high thermal resistance of BFRP bars [1,33].

Turning to details, for the beams tested at 25 °C, the ultimate load of the beam reinforced with BFRP bars increased by 11.94% compared with that of steel beams, by 14.13% compared with that of the (2S-1B) beam, and by 10.57% compared with that of the (1S-2B) beam. Also, the rate of reduction in load capacity of the BFRP beam due to exposure to high temperature (500 °C) was small, i.e. 6.17%, compared with that of the steel beam, i.e. approximately 22.32%. Consequently, the BFRP beam recorded the best reduction factor for the failure load upon exposure to fire.

It is also worth pointing out that the increase in the percentage of BFRP bars resulted in a higher value of the corresponding deflection before and after fire exposure as the steel RC beams show the smallest values of deflection in the range of 15.48–16.45 mm, the BFRP RC beams show the greatest deflection values in the range of 26.5–26.8 mm, while the hybrid RC beams show deflection values in the middle ranging between 19.44 and 22.74 mm and the reason of that match well with aforementioned in the literature,

The cracked moment of inertia in basalt-reinforced beams is approximately four times smaller than that in beams with steel reinforcement. For which, the serviceability analysis reveals significantly higher strains in concrete, beam deflections, and width of cracks [17,18]. Therefore, when the structure needs to satisfy a requirement of high flexural capacity with a requirement of low deflection, it could be suggested to use a hybrid RC beam with a suitable studied reinforcement ratio.

4.2. Crack pattern and failure mode

Fig. 8 shows the crack development and failure type for all tested beams before and after fire exposure. In general, cracking began with initial cracks in the middle section of all tested beams. As the load increased, the cracks increased in length and width, approaching both

Table 2
Steel Reinforcing Properties.

Bar No.	Area (mm^2)	Elastic Tensile Modulus (GPa)	Yield Tensile Strength (MPa)	Tensile Strain (%)
10 mm	78	216	509	0.2
6 mm	28	200	240	0.2

Fig. 1. Shimadzu Machine.

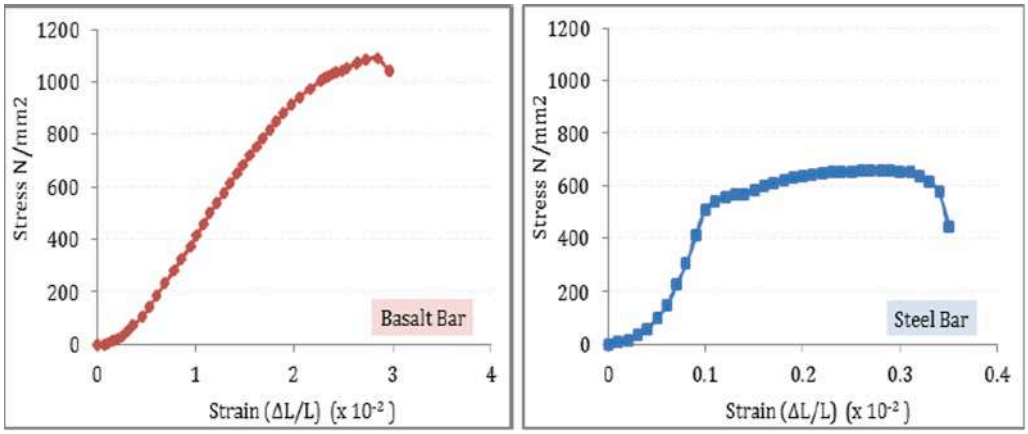

Fig. 2. Stress-Strain Curve for Basalt Bar and Steel Bar.

Table 3
Properties of the BFRPs bars.

Technical Properties	Technical Requirements	Test Results
Tensile Strength (MPa)	≥750	1450
Thermal Expansions Coeff.	9:12	10
Density (g/cm^3)	1.9:2.1	2.05
Modulus of Elasticity (MPa)	≥4.0 × 10^3	4.65 × 10^3

supports where they became inclined. Before fire exposure, the beams reinforced with a high percentage of BFRP bars showed narrower and more flexural cracks than those with steel reinforcement as the BFRP bars had lower elastic modulus and exhibited a higher strain than the steel bars. Unlike the beams reinforced with full BFPR bars, those reinforced with steel bars failed in flexure. Furthermore, the BFRP beam failed in shear with a rupture of BFRP bars near the right support, indicating that the BFRP bars have lower shear strength than the steel bars and this is expected due to the anisotropy behaviour of FRP materials which causes the dowel action of BFRP bars to be always less than that of steel bars.

After fire exposure, as the BFRP bars percentage increased, wider and fewer flexural cracks developed compared to the room beams, owing to the reduced strength of concrete and the susceptibility of the resin on the surface of the BFRPs to soften, thereby resulting in a lower bond between reinforcement and surrounding concrete [34], concrete in the compression zone crushed and the concrete cover spalled, the concrete spalling behaviour occurs in the condition of fire due to the low permeability of concrete, which limits the ability of water vapor to escape from the pores, this results in inducing internal pore pressure and thermal stresses [35]. Therefore, using a combination of steel bars and BFRP bars at normal and high temperature improves the serviceability and increases the contribution of concrete to tension stiffening through

Table 4
Reinforcement Details of Beam Specimens Prepared in This Study.

Group No.	Degree of Fire	Name of specimen	Reinforcement Type	Vertical stirrups	Main Reinforcement
G1	Room temperature 25 °C	S	Steel 3	8 Ø6 /m	3Ø10 S
		2S-1B	Steel 2 + BFRP 1	8 Ø6 /m	2Ø10 S + 1Ø10 B
		1S-2B	Steel 1 + BFRP 2	8 Ø6 /m	1Ø10 S + 2Ø10 B
		B	BFRP 3	8 Ø6 /m	3Ø10 B
G2	Fire at 500 °C (2 Hours)	S-500	Steel 3	8 Ø6 /m	3Ø10 S
		2S-1B-500	Steel 2 + BFRP 1	8 Ø6 /m	2Ø10 S + 1Ø10 B
		1S-2B-500	Steel 1 + BFRP 2	8 Ø6 /m	1Ø10 S + 2Ø10 B
		B-500	BFRP 3	8 Ø6 /m	3Ø10 B

Where: (S) Beam with Steel bars, (B) Beam with Basalt bars, (1, 2) Bars count, (500 °C) Degree of fire

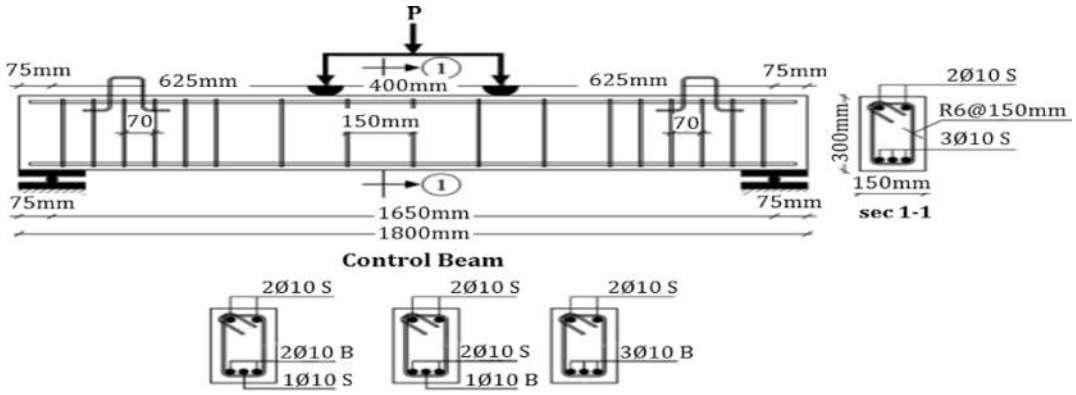

Fig. 3. Cross-Section Details of Tested Beams.

Fig. 4. Details of Reinforcement and Wooden Forms.

Fig. 5. Beams, Cubes, and Cylinders subjected to Fire.

reducing the developed strain in BFRP bars which led to minimizing the crack width and enabling more balanced flexural and shear behaviour of the RC beam.

4.3. Load deflection curve

Fig. 9 shows the relationship between the applied load and mid-span deflection for the studied beams, most of the tested beams failed in a ductile manner with large mid-span deflection thus absorbing more energy during failure. The deflections of all beams increased uniformly during loading. As shown, the behaviour of the load–deflection curve of the steel-reinforced beam can be categorized into three sections. The first section pertains to before cracking, the second section pertains to after cracking and before yielding, and the third section pertains to the

Fig. 6. Experimental Test Setup, Load Cell, and Data Logger and Reader.

Table 5
Summarised Results for Beams Reinforced Using Steel and BFRP Bars at 25 °C and 500 °C.

Type of Main Rebar	Specimen Name	First Crack Stage		Failure Stage		P_f / P_{cr}	Δ_f / Δ_{cr}	Failure Mode
		P_{cr} (kN)	Δ_{cr} (mm)	P_f (kN)	Δ_f (mm)			
3Ø10 S	**Steel**	41.22	1.326	120.5	15.48	2.60	11.70	Flexural Failure
	Steel 500°c	38.80	1.403	98.51	16.45	2.47	11.67	Flexural Failure
2Ø10 S + 1Ø10 B	**2S-1B**	39.43	1.543	118.2	19.44	3.00	12.60	Flexural Failure
	2S-1B 500 °C	33.94	1.752	95.48	19.98	2.70	11.40	Flexural Failure
1Ø10 S + 2Ø10 B	**1S-2B**	42.53	1.743	122.00	19.85	2.90	11.40	Flexural Failure
	1S-2B 500 °C	39.93	2.45	106.85	22.74	2.67	9.30	Flexural Failure
3Ø10 B	**Basalt**	47.74	1.832	134.89	26.518	2.83	10.67	Shear Failure
	Basalt 500 °C	43.38	2.69	127.06	26.824	2.93	9.97	Flexural Failure

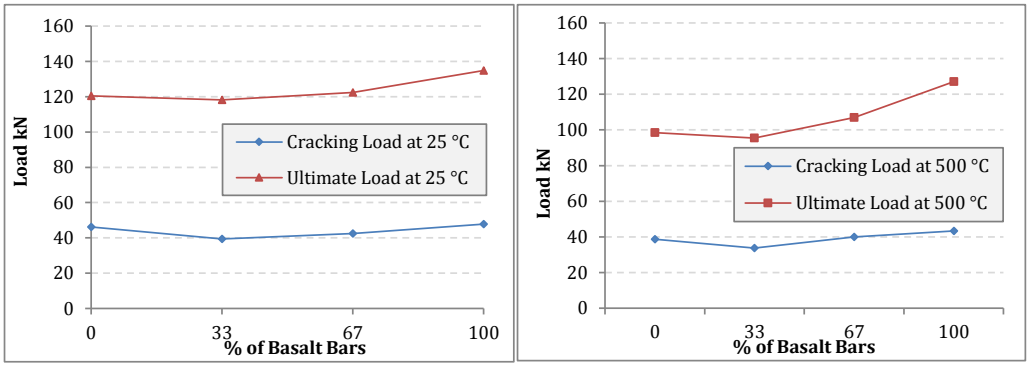

Fig. 7. Effects of BFRP Bars on Cracking and Failure load at 25 °C and 500 °C.

yielding of the main reinforcement until failure. Whereas the load deflections curve of the BFRP reinforced beam was linear before cracking and slightly nonlinear up to failure with lack of yielding.

The largest deflection and load in two groups (at 25 °C and 500 °C) were achieved in the reinforcement beam with only BFRP bars and the only RC steel beam exhibited lower deflection values particularly before the yielding stage, while the deflection of hybrid beams were approximately 50% and 73% when compared to only BFRP RC beams at service and ultimate load respectively. This is owing to the low elastic modulus of the FRP, as the deflection of a beam varies inversely with the modulus of elasticity, this can result in a considerable amount of deflection compared with the only steel RC beam, even for the same value of the load. The increased deflection will lead to extensive cracking along the length of the beam, thereby significantly reducing its flexural stiffness. So the stiffness of steel RC slightly reduced after cracking, but the stiffness of the BFRP RC beam obviously decreased after cracking, whereas the beams with different ratios of steel and BFRP bars were between them.

The effect of high temperatures was evident from the continuous decrease in the load capacity of the beams. This decay was relative to the BFRP bar ratio in the reinforced beams as the load capacity of the steel-reinforced beam was more pronounced than those obtained with 33%, 67%, and 100% of BFRP bars. Consequently, the decrease in failure load was 6–23% compared with that of normal beams at 25 °C, owing to the lower thermal conductivity of the BFRP bars as well as BFRP bars have almost the same thermal coefficient of expansion as concrete [2].

4.4. Strains in tension bars under load

The beams reinforced with steel and BFRP bars exhibited different axial strains; however, the beam reinforced with steel bars demonstrated a higher strength than that reinforced with 100% BFRP bars (B). However, when BFRP bars were added at a ratio of 33% (2S-1B), the beam strength was similar to that of reinforced steel bars (S) but with higher strains. When FRP bars were added at a ratio of 67% (1S-2B), the beam strength was similar to that of reinforced fiber bars (B), with similar strains as well, as shown in Fig. 10.

It is clear that the steel bars have a lower strain than the basalt bars, in particular before the yielding stage. After cracking, the steel-reinforced beams were much stiffer than the BFRP-reinforced beams. The failure strain of the BFRP bars was $\frac{1450}{46500} = 0.0312$, whereas the average maximum strain at beam failure was 0.023. This clearly indicates that the fracture of the BFRP bars was not due to the axial

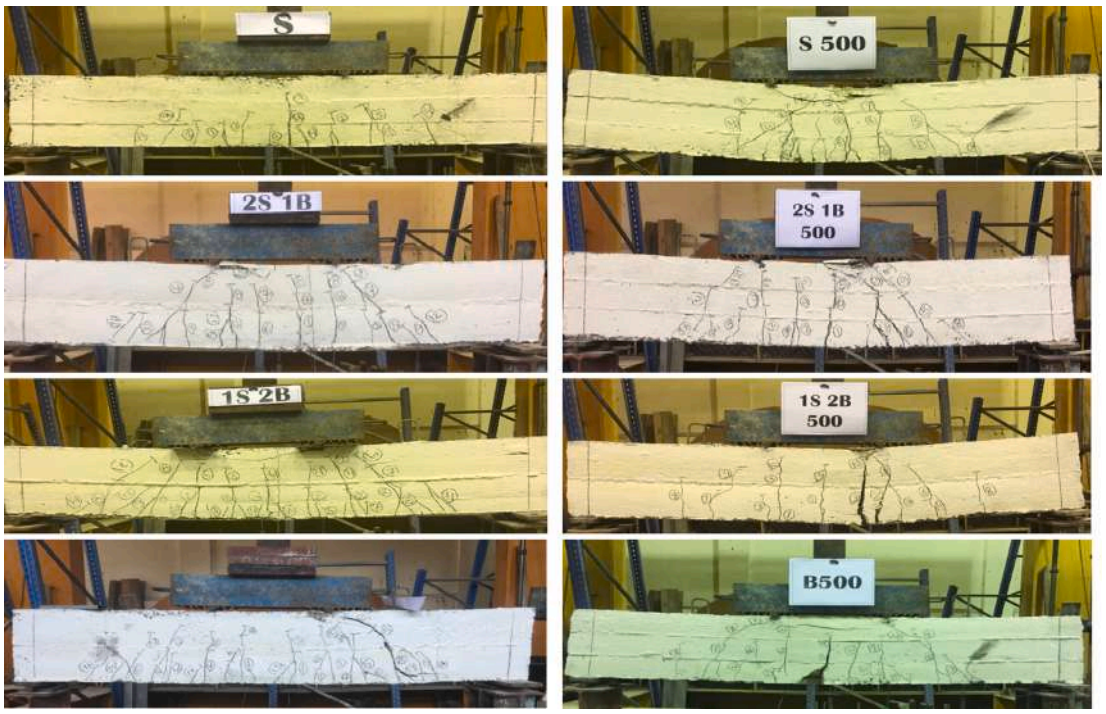

Fig. 8. Cracks and Failure Mode of Tested Beams.

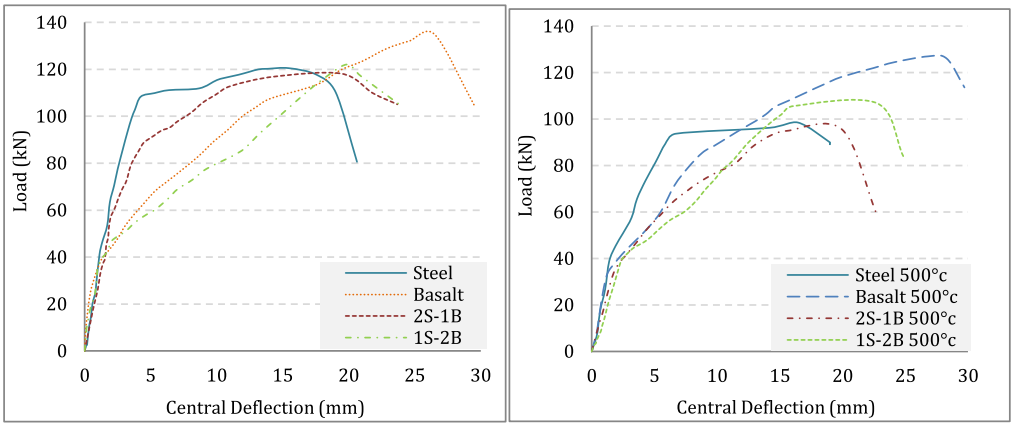

Fig. 9. Load–Deflection Curves at Mid Span for Beams Tested at 25 °C and 500 °C.

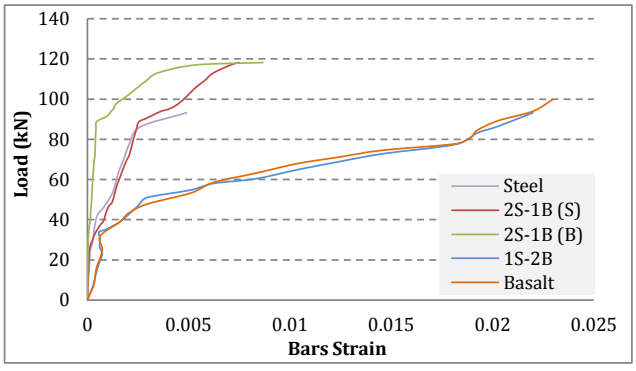

Fig. 10. Load–Strain Curves for Beams Tested at 25 °C.

loading of the bars and that they were subjected to multi-axial stresses, which caused them to fail prematurely, possibly due to dowel action. The yield strain of the steel bars was $\frac{360}{200000} = 0.0018$, which agrees reasonably well with the values of strain corresponding to the yielding of the steel-reinforced beams (see Fig. 11).

4.5. Stiffness, ductility index, and absorbed energy

The stiffness, ductility index, and absorbed energy for all tested beams are shown in Table 6. Two values of stiffness were estimated: the initial stiffness (K_i), which is defined as the slope of the load–deflection curve at the beginning of the test at values before the load cracks; and the stiffness after cracking (Ks), which is defined as the slope of the load–deflection curve at the elastoplastic zone.

Ductility is the ability of a material to endure extreme plastic deformations before rupture or breaking. It is calculated as the ratio of the maximum displacement to the first yield displacement (Δ_{max}/Δ_y). The first yield displacement Δ_y corresponds to the intersection of tangents to the load–displacement curve at the origin and the maximum

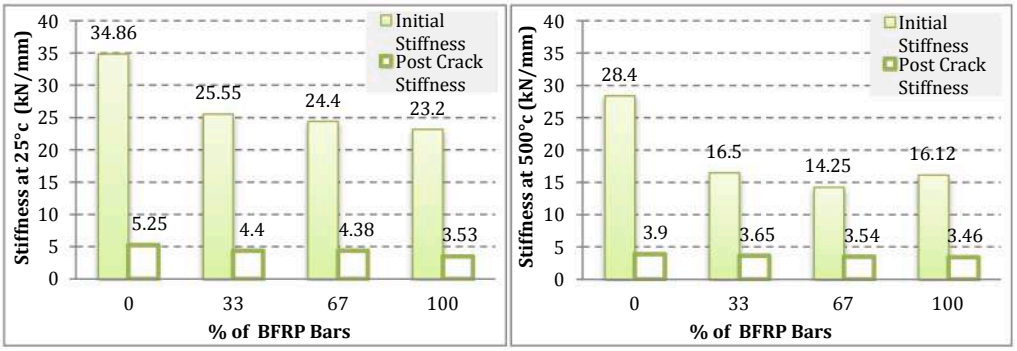

Fig. 11. Initial and Post Crack Stiffness for Specimens at 25 °C and 500 °C.

Table 6
Stiffness, Ductility Index, and Absorbed Energy.

Group No.	Specimenname	Initial Stiffness (Ki) (kN/mm)	Post Crack Stiffness (Ks) (kN/mm)	Ductility Index	Absorbed Energy kN·mm
G. 1 (25 °C)	S	34.86	5.25	4.60	2126.45
	2S-1B	25.55	4.50	6.10	1586.69
	1S-2B	24.40	4.38	7.00	1540.03
	B	23.20	3.50	8.80	938.285
G. 2 (500 °C)	S-500	28.40	3.90	3.67	1558.86
	2S-1B-500	16.50	3.65	5.00	987.60
	1S-2B-500	14.24	3.54	5.80	877.00
	B-500	16.12	3.46	7.40	578.64

displacement.

The energy absorption based on displacement is the ability of a material to absorb energy prior to failure; it is evaluated as the area under the load–deflection curve until the failure load.

The initial and post-crack stiffness of all beams were calculated, as shown in Table 5 and Fig. 8. At room temperature, all beams recorded a lower initial stiffness than the control beam, and the BFRP beam indicated an initial stiffness that was 33% lower than that of the steel beam. Furthermore, at high temperatures, the initial stiffness of the BFPR beam was 43% lower than that of the steel beam.

The ductility of the steel and BFRP reinforcement beams differed depending on the ratio of BFRP bars added, as shown in Figs. 9 and 10. The beams with a high percentage of BFRP bars indicated a high ductility comparable to that of steel beams at 25 °C and 500 °C as the steel beams ductility were lower than the BFRP beams by 52.27% and 50.50% at 25 °C and 500 °C, respectively. Additionally, the reduction factor of the ductility index for the tested beams after exposure to fire was calculated. It was observed that the reduction factor of the BFRP beam was 16%. This indicates that the BFRP bars have a higher efficiency than the steel bars when subjected to fire.

Table 5 and Fig. 10 show that the maximum energy absorption capacity was achieved for the BFRP beam at the two studied temperatures. This is because the BFRP bars can support high tensile stress while achieving a high strain in the tension zone; consequently, the energy absorption capacity improved.

5. Finite element analysis

The aim of the numerical investigation is to get a reliable method for predicting the behaviour of the tested beams at room temperature (G1). ANSYS parametric design language program (APDL) was used to simulate the tested beams, and the results obtained are compared with the experimental results. SOLID65 was used to model concrete. SOLID65 is an eight-node solid element and has three displacements and three rotation degrees of freedom at each node; it requires linear and nonlinear isotropic material properties. LINK180 was used to model the steel and BFRP reinforcements; it requires linear and bilinear isotropic material properties. This element is a three-dimensional link element with two nodes and three degrees of freedom translations in the nodal x, y, and z directions as listed in Table 6 and Table 7. The bond between the concrete and reinforcement was considered perfect. SOLID185 was used to simulate the loading and support plates in ANSYS (SAS 2012) [36]. Table 11 presents the experimental, analytical, and theoretical results for the room temperature beams (see Table 8).

The beam, plates, and supports were simulated as volumes. The overall mesh of the reinforced concrete beam, plate, and support volumes is shown in Fig. 12. The merge items command was used to join separate parts that were at the same position (see Table 9).

5.1. Nonlinear solution

A nonlinear structural behavior may arise because of geometric and material nonlinearities. Geometric nonlinearities refer to the nonlinearities due to the changing geometry as it deflects, while material nonlinearities occur due to the nonlinear relationship between stress and strain. In this model material nonlinearities considered. The total load applied to a finite element model is divided into a series of load increments called load steps. At the end of each incremental solution, the stiffness matrix of the model is adjusted to reflect nonlinear changes in structural stiffness before continuing to the next load increment. Newton-Raphson equilibrium iterations were used for updating the model stiffness [36].

Table 7
Material Properties for Concrete Element.

Linear Isotropic		Multi-linear Isotropic		Concrete	
EX	24,870	stress	strain	βo	0.30
PRXY	0.20	0.000323	8.40	βc	0.90
‘		0.001	21.0	fr	3.67
		0.0015	26.3	fc'	28.0
		0.002	28.0		
		0.003	28.0		

Table 8
Material Properties for LINK180 and SOLID185 Elements.

2.LINK180 Basalt Bar	Linear Isotropic			
	EX	46,500		
	PRXY	0.26		
3.LINK180 Steel Bar	Linear Isotropic	Bilinear Isotropic		
	EX	$2*10^5$	Yield Stress	360
	PRXY	0.30	Tang Mod	0.00
4.LINK180 Stirrup	Linear Isotropic	Bilinear Isotropic		
	EX	$2*10^5$	Yield Stress	240
	PRXY	0.30	Tang Mod	0.00
5.SOLID 185	Linear Isotropic			
	EX	$2*10^5$		
	PRXY	0.30		

5.2. Crack pattern

The ANSYS program showed a crack pattern at each applied load. Cracking is represented with a circle set in the plane of the crack, whereas crushing is represented by drowning with an octahedron outline. The first crack at the integration point is shown with a red circle, the second crack with a green circle, the third crack with a blue circle, and closed cracks with an X inside the circle. The ANSYS program shows compression, flexural, diagonal, and tensile cracks. From Fig. 13 The crack patterns of the simulated beams at the last converged load step coincide well with that from experimental work as the beams with a higher percentage of basalt bars show more developed cracks along the span of the beams while steel beam flexure cracks concentrated in the middle of the beam (see Fig. 14).

5.3. Stress distribution

The finite element program depicts stresses at the integration points of solid elements. The maximum nodal stresses in concrete and the nodal stresses in the steel reinforcement and BFRP bars were obtained at the last converged load step and shown in form of contour lines, as depicted in Fig. 15, for the steel beam and BFRP beam models. From figure, it's clear that more stresses developed in the shear zone for the basalt beams while the steel beams showed stress concentration in the flexural zone and this match with the failure mode from experimental work (see Figs. 16–18).

6. Theoretical calculation according to ACI code

For a simply supported beam loaded by two-point loads, the maximum deflection Δ_{max} can be calculated as follows:

$$\Delta_{max} = \frac{pa}{24EI_e}(3l^2 - 4a^2) \quad (1)$$

Owing to the higher stiffness of the steel reinforcement, the gradual transition from the gross moment of inertia to the cracked moment of inertia is relatively slower. This is consistent with the effective moment of inertia based on the original Branson's equation as follows:

$$I_e = \left(\frac{M_{cr}}{M_a}\right)^3 \times I_g + \left[1 - \left(\frac{M_{cr}}{M_a}\right)^3\right] \times I_{cr} \le I_g \quad (2)$$

The transition of the gross moment of inertia of the BFRP reinforced beam to the cracking moment of inertia is faster than that of the steel-reinforced beam; consequently, the deflection response due to the original Branson's equation is stiffer and exhibits a slower degradation. The ACI Committee 440.1R-06 suggested an amendment to the original Branson's equation such that the reduction coefficientβ_d is incorporated

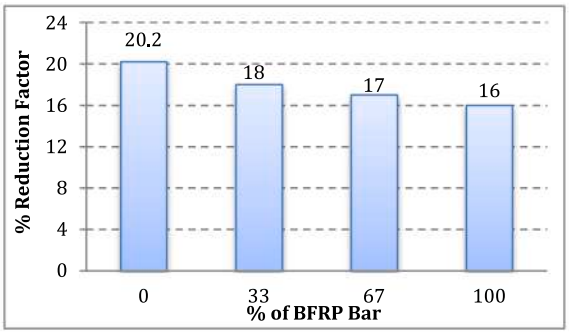

Fig. 13. Reduction Factor of Ductility Index According to BFRP bar Reinforcement Ratio.

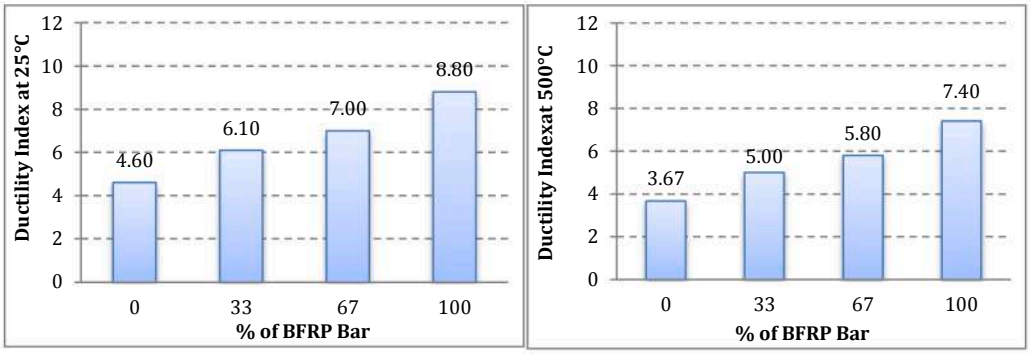

Fig. 12. Measurement of Ductility for Specimens at 25 °C and 500 °C.

Table 9
Theoretical Deflection Calculations.

Beam	β_d	I_g mm^4	I_{cr} mm^4	M_{cr} kN·m	M_a kN·m	M_{cr}/M_a	I_e mm^4	Δmm
Steel	–	$3.375*10^8$	8.06×10^7	8.44	32.00	0.264	9.633×10^7	7.53
2S-1F	0.256	$3.375*10^8$	7.11×10^7	8.07	39.93	0.202	8.344×10^7	11.26
1S-1F	0.513	$3.375*10^8$	4.93×10^7	7.87	42.66	0.184	6.971×10^7	17.11
BFRP	0.770	$3.375*10^8$	2.53×10^7	7.65	42.70	0.179	5.806×10^7	32.17

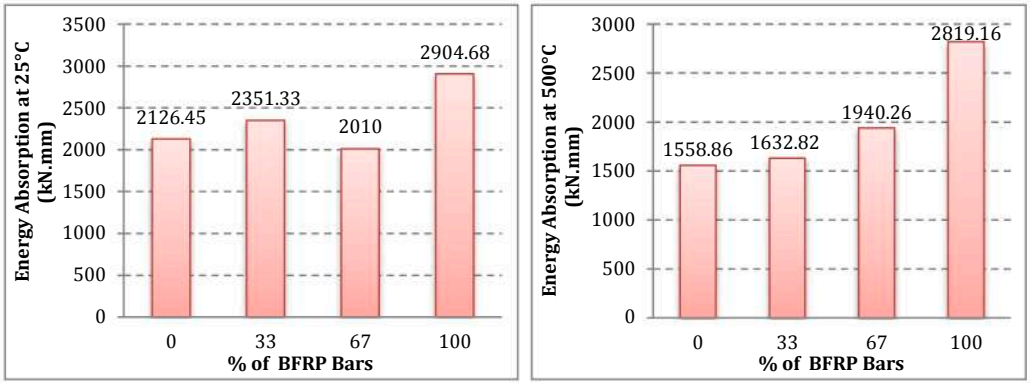

Fig. 14. Absorbed Energy of Specimens at 25 °C and 500 °C.

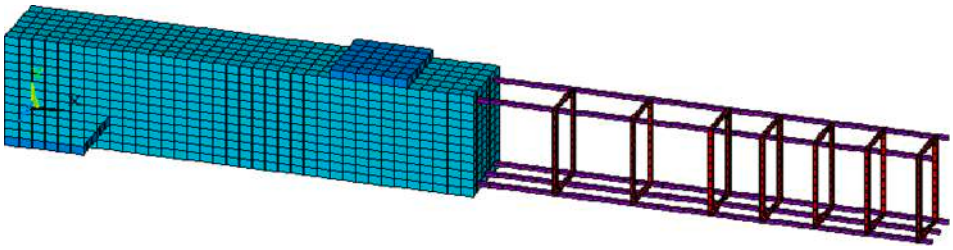

Fig. 15. FE Model of Tested Beam.

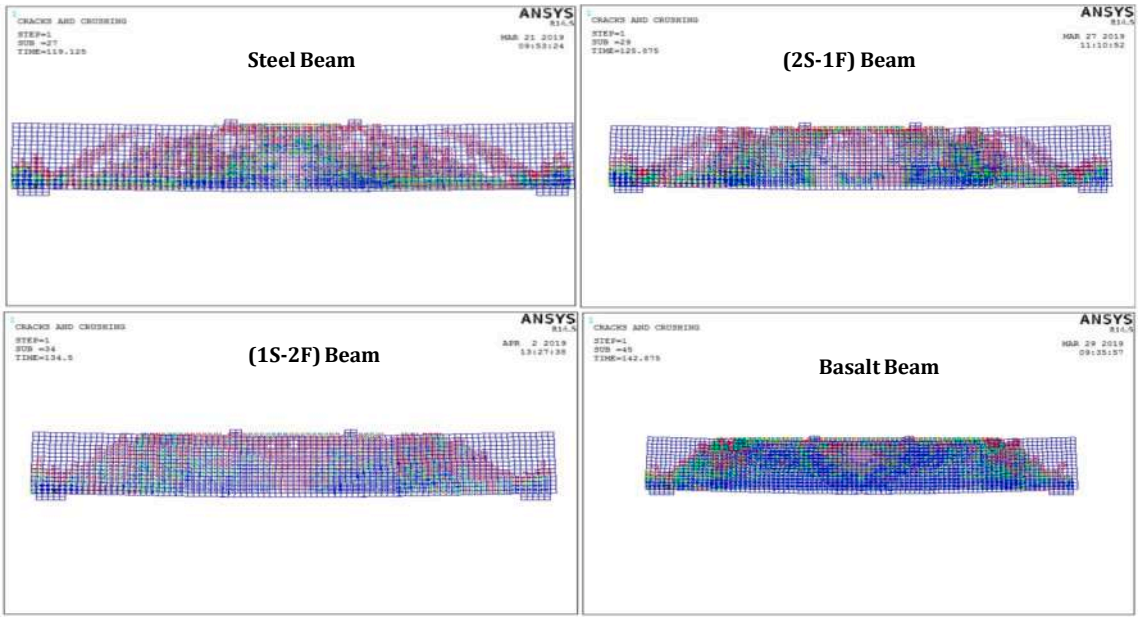

Fig. 16. Crack Patterns of Modelled Beams.

to include the effect of the reinforcement ratio on the deflection analysis of the FRP-reinforced beams.

$$I_e = \left(\frac{M_{cr}}{M_a}\right)^3 \times \beta_d \times I_g + [1 - \left(\frac{M_{cr}}{M_a}\right)^3] \times I_{cr} \leq I_g \quad (3)$$

$$\beta_d = \frac{\rho_f}{5 \times \rho_{fb}} \leq 1 \quad (4)$$

$$\rho_{fb} = 0.85 \times \beta_1 \times \frac{f_c^{'}}{f_{fu}} \times \frac{E_f \times \varepsilon_{cu}}{E_f \times \varepsilon_{cu} + f_{fu}} \quad (5)$$

where

ρ_{fb}: balanced reinforcement ratio of FRP beams
β_1 : Factor depending on concrete strength
$f_c^{'}$: Concrete compressive strength from cylinder test
E_f :Longitudinal modulus of elasticity of FRP
ε_{cu} : Ultimate compressive strain of concrete (typically set as 0.003)

$$M_u = f_f \times A_f \times \left(d - \frac{a}{2}\right) \quad (6)$$

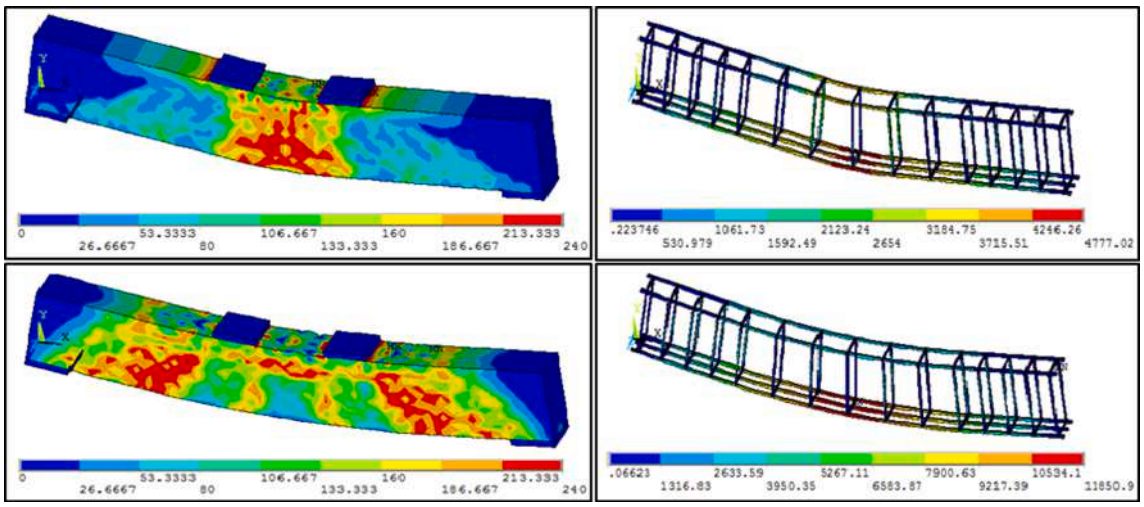

Fig. 17. Stress in Concrete and Stress in Reinforcement for Steel Beam and BFRP Models.

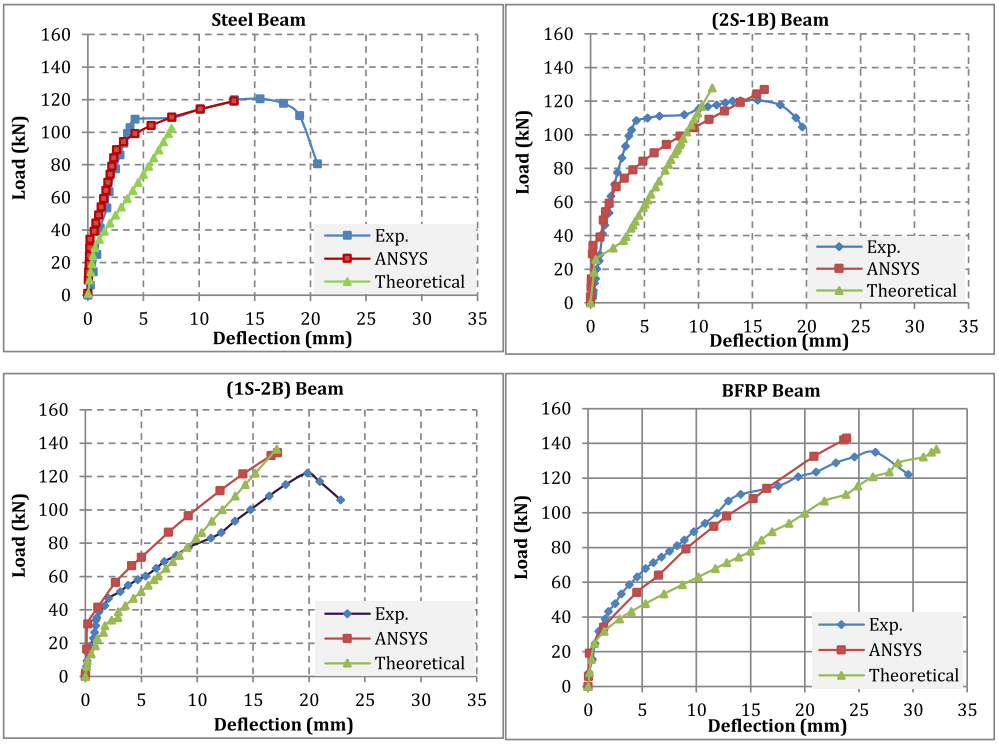

Fig. 18. Load–Deflection Curves for Tested Beams.

$$a = \frac{A_f \times f_f}{0.85 \times f_c^{'}} \times \frac{(E_f \times \varepsilon_{cu})^2}{4} \tag{7}$$

$$f_f = \sqrt{\frac{(E_f \times \varepsilon_{cu})^2}{4} + \frac{0.85 \times \beta_1 \times f_c^{'}}{\rho_f} \times E_f \times \varepsilon_{cu}} - 0.5 \times E_f \times \varepsilon_{cu}, \tag{8}$$

where a is the depth of the stress block, d the effective depth of the section, b the width of the beam, and A_f the cross-sectional area of the FRP bar. The theoretical deflection calculations of all tested beams at mid-span according to ACI 440.1R-06 [1] are shown in the next table.

7. Results of numerical simulation and theoretical calculation

Table 10 shows results from the experimental, finite element, and

Table 10
Experimental, Analytical, and Theoretical Results for Tested Beams.

Specimens	Experimental		Analytical		Theoretical	
	Pul (kN)	Δul (mm)	Pul (kN)	Δul (mm)	Pul (kN)	Δul (mm)
Steel	120.49	15.48	119.12	13.14	102.4	7.53
2S-1B	118.13	19.44	126.88	16.10	127.77	11.26
1S-2B	122.00	19.85	134.50	17.18	136.51	17.11
Fibre	134.89	26.52	142.88	23.88	136.61	32.17

theoretical calculations according to ACI 440.1R-06 [1] at the failure stage.

7.1. Load–deflection behaviour

The experimental and finite element analysis load–deflection curves as well as those obtained by ACI computation for beams reinforced with different ratios of BFRP are shown in Fig. 15. From the curves obtained, it is clear that the ANSYS simulation results agreed better with the experimental results than the theoretical results, as the latter indicated a lower stiffness than the other curves. In fact, after cracking, the actual stiffness of the beam is between the gross-stiffness (E_cI_g) and cracked-stiffness (E_cI_{cr}); however, in the theoretical equations, once the concrete cracked and reached its rupture strength, the effect of the concrete on the extreme tensile fiber was neglected; hence, the slope of the load–deflection curve reduced significantly.

8. Conclusions

The conclusions of this study are as follows:

1. The greater the fraction of BFRP bars, the higher was the cracking along the length of the beam and the corresponding deflection, owing to their lower elastic modulus
2. The BFRP beam indicated an initial stiffness that was lower by 33% and by 43% compared with those of the steel beam at room and high temperatures, respectively.
3. The beams with a high percentage of BFRP bars indicated high ductility, whereas the steel beam at 25 °C and 500 °C recorded a ductility that was lower by 52.27% and 50.50% compared with the beam reinforced only with BFRP respectively. This indicates that the BFRP bars had higher efficiency than the steel bars when subjected to fire.
4. At the two studied temperatures, the BFRP beam achieved the greatest energy absorption capacity as the BFRP bars were able to support high tensile stresses while achieving a high strain in the tension zone; consequently, the energy absorption capacity enhanced.
5. The numerical results from finite element modelling and the theoretical calculation according to the ACI agreed reasonably well with the experimental results in terms of the ultimate load and deflection.
6. Using both the steel and BFRP bars in the same beam improved serviceability and enhanced the crack pattern, cracked stiffness, and the failure mode of the tested beam at both studied temperatures.
7. By controlling the percentage of hybrid reinforcement, a reasonable deflection, crack width and stiffness could be achieved and accordingly satisfying serviceability requirements.

Declaration of Competing Interest

The authors declare that they have no known competing financial interests or personal relationships that could have appeared to influence the work reported in this paper.

References

[1] ACI 440. Guide for the Design and Construction of Structural Concrete Reinforced with FRP Bars, American Concrete Institute Farmington Hills, MI; 2006..
[2] Subramanian N. Sustainability of RCC Structures Using Basalt Composite Rebar. Gaithersburg, MD, USA; September, 2013.
[3] Barris C, et al. An experimental study of the flexural behaviour of GFRP-RC beams and comparison with prediction models. Compos Struct 2009;91(3):268–95.
[4] Inman M, Thorhallsson ER, Azrague K. A mechanical and enviromental assessment and comparison of basalt fiber reinforced polymer (BFRP) rebar and steel rebar in concrete beams. Energy Procedia 2017;111:31–40.
[5] Fiore V, Di Bella G, Valenza A. Glass-basalt poxy hybrid composites for marine applications. Mater Des 2011;32(4):2091–9.
[6] Urbanski M, Lapko A, Garbacz. Investigation of concrete beams reinforced with basalt rebars as an effective alternative of conventional RC structures. Proc Eng 2013;57:1183–91.
[7] Bank L. Composites for construction, structural design with FRP materials; 2006.
[8] Artmenko SE. Polymer composite material made from carbon, basalt, and glass fibers. Struct Prop, Fibre Chem 2003;35(3):226–9.
[9] Wei B, Cao H, Song S. Environmental resistance and mechanical performance of basalt and glass fibres. Mater Sci Eng 2010;527(18):4708–15.
[10] Borhan TM. Properties of glass concrete reinforced with short basalt fibre. Mater Des 2012;42:265–71.
[11] Sim Jongsung, Park Cheolwoo. Do Young Moon, Characteristics of basalt fiber as a strengthening material for concrete structures. Compos B 2005;36:504–12.
[12] Kabay N. Abrasion resistance and fracture energy of concrete with basalt fibre. Constr Build Mater 2014;50:95–101.
[13] Branston J, et al. Mechanical behavior of basalt fiber reinforced concrete. Constr Build Mater 2016;124:878–86.
[14] Elgabbas F, Ahmed EA, Benmokrane B. Physical and mechanical characteristics of new basalt FRP bars for reinforcing concrete structures. Constr Build Mater 2015;95:623–35.
[15] Branson ED. Deformation of Concrete Structures / Dan E. Branson; 2018.
[16] Almeida Junior Salvio Aragao, Parvin Azadeh. Behaviour Of Continuous Concrete Beams Reinforced With Basalt Bars, Interdependence between Structural Engineering and Construction Management; 2019, STR-66-1.
[17] Bank LC. Progressive failure and ductility of FRP composites for construction: review. J Compos Constr 2013;17(3):406–19.
[18] Sim J, Park C, Moon DY. Characteristics of basalt fiber as a strengthening material for concrete structures. Compos B Eng 2005;36(6):504–12.
[19] Wei Shi J, et al. Durability of BFRP and hybrid FRP sheets under Freeze-Thaw Cycling. 2010;163–167:3297–3300.
[20] Youssef T, El-Gamal S, Benmokrane B Long term deflection of GFRP-reinforced concrete beams under uniform sustained load. 2009;3:1617–25.
[21] Toutanji H, Deng Y. Deflection and crack-width prediction of concrete beams reinforced with glass FRP rods. Constr Build Mater 2003;17(1):69–74.
[22] Bischoff PH. Re-evaluation of deflection prediction for concrete beams reinforced with steel and fiber reinforced polymer bars. J Struct Eng 2005;131(5):752–67.
[23] Patnaik A, et al. Mechanical properties of basalt fiber reinforced polymer bars manufactured using a wet layup method 2012;3:412–17.
[24] Patnaik DA. Applications of Basalt Fiber Reinforced Polymer (BFRP) Reinforcement for Transportation Infrastructure. Developing a Research Agenda for Transportation Infrastructure - TRB November; 2009.
[25] Hassan A, Khairallah F, Mamdouh H, Kamal M. Evaluation of self-compacting concrete columns reinforced with steel and FRP bars with different strengthening techniques. Structures 2018.
[26] Hassan A, et al. Use of carbon nanotubes in the retrofitting of reinforced concrete beams with an opening and the effect of direct fire on their behaviour. Int J GEOMATE 2018;14(44).
[27] Elkady H, Hassan A. Assessment of high thermal effects on carbon nanotube (CNT)-reinforced concrete. Sci Rep 2018;8(1):11243.
[28] American Concrete Institute. Guide for Determining the Fire Endurance of Concrete Elements. ACI 216R-89.
[29] EN 1992-1-2: Euro-code 2, Design of Concrete Structures. Part 1.2: General Rules – Structural Fire Design, p. 97, December; 2004.
[30] Hassan A, et al. Evaluation of self-compacting concrete columns reinforced with steel and FRP bars with different strengthening techniques. Structures 2018;15:82–93.
[31] Elkady H, Hasan A. Protection of reinforced concrete beams retrofitted by carbon fibre-reinforced polymer composites against elevated temperatures. Can J Civ Eng 2010;37(9):1171–8.
[32] ECP 203. Egyptian Code for Design and Construction of Concrete Structures. Housing and Building National Research Center, Cairo, Egypt; 2018.
[33] ECP, 208. Egyptian Code for the Use of Fiber Reinforced Polymers in the Construction Field. Housing & Building National Research Center, Cairo, Egypt; 2005.
[34] Hamad RJA, Megat Johari MA, Haddad RH. Mechanical properties and bond characteristics of different fiber reinforced polymer rebars at elevated temperatures. Constr Build Mater 2017;142:521–35.
[35] Kalifa, Menneteau FD, Quenard D. Spalling and porepressure in HPC at high temperature. Cement Concr Res 2000;1:1915–27.
[36] ANSYS. ANSYS Help. Release 14.5, Copyright; 2012.